(Preprint) AAS 13-707

OPTICAL SENSOR CONSTRAINTS ON SPACE OBJECT DETECTION AND ADMISSIBLE REGIONS

Johnny L. Worthy III[*], Marcus J. Holzinger[†], Kohei Fujimoto[‡]

This paper presents work on a model to simulate the space debris environment based on optical sensor detection constraints of line of sight, illumination, and visual magnitude. Through analysis, the performance of pointing trajectories, such as the automated sensors in the Space Surveillance Network (SSN), can be optimized based on the shapes of these constraints. This application is particularly of interest to space based sensors and the design of space based space surveillance missions. The presented constraints are also found to be dependent on range to the space object. This dependence is used to apply additional constraints to the admissible region further aiding in initial state estimation of space objects observed from space.

INTRODUCTION

Space situational awareness is becoming a primary area of interest for organizations such as NASA and United States Strategic Command (USSTRATCOM). The increase in spacecraft launches since 1957 has led to growing population of satellites, rocket bodies, and debris in orbit around Earth. With a constantly changing population, identifying and tracking these objects is necessary in order to maintain the safety of high value assets in orbit and to predict and detect when collisions occur between objects. The Space Surveillance Network (SSN) is a crucial part of the current space object detection and tracking strategy. A network of 29 phase-array radars, conventional radar, electro-optical sensors, and space-based sensors comprise the SSN [1]. Between 380,000 and 420,000 observations are made daily using predictive techniques to automate object targeting and tracking. These predictive techniques are based on known debris distribution models which help optimize the observation strategy [2]. The current technology used by the SSN can detect objects down to approximately 10cm in size. Objects smaller than 10 cm are much more difficult to detect due to Raleigh scattering [3].

New launches, collisions, fragmentation, material degradation, and object deorbit all contribute to the change in the catalog size over time; however, it is estimated that there are over 300,000 objects in LEO larger than 1 cm [4]. Information on all objects identified is collected in a database maintained by the Joint Space Operations Center (JSpOC) which then makes publicly available all unclassified objects' information. Currently it is estimated that of the objects cataloged, only approximately 7% are functional payloads and satellites [5]. The other 93% of space objects, along with the estimated hundreds of thousands of objects currently untracked, pose the largest threat. According to NASA's characterization of space object collisions, interactions between objects larger

[*]Undergraduate Researcher, School of Aerospace Engineering, Georgia Institute of Technology
[†]Assistant Professor, School of Aerospace Engineering, Georgia Institute of Technology.
[‡]Post-doctoral Research Associate, Aerospace Engineering, Texas A&M

than 10 cm are potentially catastrophic and interactions between objects between 1 cm and 10 cm have the potential to disable or disrupt a mission. Such was the case during the collision of the Iridium 33 and Cosmos 2251 satellites in 2009. This event resulted in the loss of both satellites and the addition of 1,632 new debris objects into the catalog as of 1 December 2009 [6].

Reducing the risk of such potentially catastrophic collisions, requires more and higher quality data on the objects being tracked. The orbital element data of tracked space objects is one of the main functions the SSN provides. Using this information, predictions can be made about where space objects will be at a given time. The spatial density of the objects in a given area are of particular interest since higher spatial density of space objects implies a higher probability of detecting an object in this area. Furthermore, by propagating forward in time and looking at how these high density regions move over time, insight can be gained which can improve the automation of sensors such as those in the SSN. The Reconnaissance of Space Objects (RECONSO) mission, a selected AFOSR UNP-8 cubesat mission currently under development at Georgia Tech, will use a passive optical sensor, similar to the one aboard SBV [7], which can ultimately benefit from having an optimized pointing trajectory in orbit. With better trajectories designed to provide maximal detectability of objects, future space surveillance efforts like the Raven class telescope under development at Georgia Tech [8] or RECONSO , can provide higher fidelity information on the space debris environment. This information would also provide the ability to comparatively assess the performance utility of different observation platforms. The optical detections of objects are usually in the form of position and velocity in angular space. The limitations in sensing capabilities, especially in space-based observations, place significant constraints on what is visible to the observer. By utilizing this fact, admissible region methods for initial orbit determination provide a method by which range and range rate estimates can be estimated based on the observation scenario. The addition of applicable constraints on the admissible regions for a given scenario further reduces the possible range and range rate solutions for a given observation.

In this paper a model is introduced which simulates the space debris environment based on the information contained in the publicly available space object catalog. Considering the detectability of objects in the catalog, a conservative 3-D volume is defined which bounds the region in which an observer can detect objects. The constraints derived are applied to the admissible region as defined by [9, 10]. Three constraints are defined which can be imposed on the admissible region; an illumination constraint defining the illumination of the object by the sun, a limiting magnitude constraint, and an inclination constraint. Finally, a simulation is presented which combines the defined constraints and visualizes where an observer can point to detect objects.

OPTICAL DETECTION OF OBJECTS

The analysis of the detectability of objects is performed using the ECI position and velocities of the objects. The ECI position of the observer is denoted as $\mathbf{o}$ and the position of the object is denoted as $\mathbf{r}$. In order for an object to be detectable to an observer, the observer must have line-of-sight (LOS) to the target, the target must be illuminated, and the object must have an apparent magnitude detectable by the sensor. The LOS vector, which connects the object and the observer, is defined as $\mathbf{v}$. The Sun vector which points from the sun to the object is denoted as $\mathbf{s}$ and the angle between $\mathbf{s}$ and $\mathbf{v}$ is defined as ψ, the solar phase angle. Lastly, the pointing direction of the observer, $\hat{\mathbf{p}}$, is used to define the angle between the object's location and the center of the observer's field of view. Figure 1 illustrates the defined coordinate system.

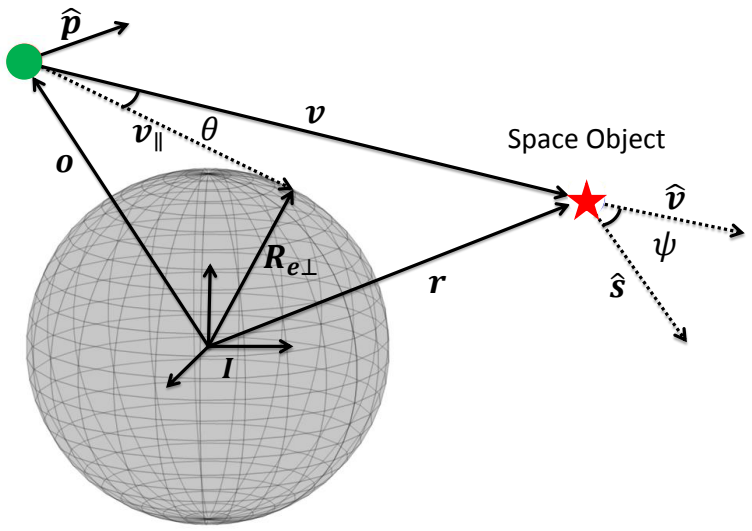

Figure 1. Definition of the coordinate system. The observer is green circle and the space object is red star.

Line of Sight

The region of space in which the observer has line of sight is a cone extending from the observer with the slope tangent to the Earth's surface. Using the notations shown in Figure 1, the minimum angle, θ, between the vector $\mathbf{v}_{\parallel}$ and $\mathbf{o}$ can be defined. The $\mathbf{v}_{\parallel}$ vector defines the location at which the LOS vector is tangent to the surface of the Earth. The Earth radius vector at this point is denoted as $\mathbf{R}_{e\perp}$. Noting the geometry shown in Figure 1 and that $\|\mathbf{R}_{e\perp}\|^2 + \|\mathbf{v}_{\parallel}\|^2 = \|\mathbf{o}\|^2$, the following equations derives the line of sight condition for an object.

$$\cos\theta = \frac{\sqrt{\|\mathbf{o}\|^2 - \|\mathbf{R}_{e\perp}\|^2}}{\|\mathbf{o}\|} \tag{1}$$

$$\mathbf{o} \cdot \mathbf{v} \geq -\cos\theta \|\mathbf{o}\| \|\mathbf{v}\| \tag{2}$$

Substituting Equation (1) into Equation (2), the inequality shown in Equation (3) is obtained. This inequality gives the LOS conditions of the objects in the simulation, marking the observer as having line of sight if true and as not having line of sight if false. As can be seen in the equation, the line of sight constraint is independent of the range to the space object.

$$\mathbf{o} \cdot \hat{\mathbf{v}} + \sqrt{\|\mathbf{o}\|^2 - \|\mathbf{R}_{e\perp}\|^2} \geq 0 \tag{3}$$

Illumination

Objects that are in the Earth's shadow cannot be seen by the observer. The illumination of an object is determined by whether or not it is in the Earth's shadow. Given the sun vector $\mathbf{s}$, an object that is eclipsed by the Earth has to satisfy the two approximate conditions shown in Equations (4) and (5), where R_e is the radius of the Earth.

$$\mathbf{r} \cdot \hat{\mathbf{s}} > 0 \tag{4}$$

$$\|\hat{\mathbf{s}} \times \mathbf{r}\| \leq R_e \tag{5}$$

Visual Magnitude

Visual magnitude is important for optical observation as it is a measure of how bright an object is. Objects that are too dim cannot be detected and thus a constraint considering object visual magnitude can be applied. The conservative approximate apparent visual magnitude for a spherical object can be calculated with Equation (8), given the range to the object ρ, the diameter of the object d, the solar phase angle ψ, and the specular and diffuse components of its reflectance a_{spec} and a_{diff} [11]. Equation (8) is supplemented with Equation (7), the diffuse phase angle function [12], which alternates the diffuse reflectance according to the objects solar phase angle calculated with Equation (6).

$$\psi = \cos^{-1}\left(\frac{\mathbf{v}\cdot\mathbf{s}}{\|\mathbf{v}\|\|\mathbf{s}\|}\right) \tag{6}$$

$$p_{\text{diff}}(\psi) = \frac{2}{3\pi}\left[\sin(\psi) + (\pi-\psi)\cos(\psi)\right] \tag{7}$$

$$m_{\text{obj}} = m_{\text{sun}} - 2.5\log\left\{\frac{d^2}{\rho^2}\left[\frac{a_{\text{spec}}}{4} + a_{\text{diff}}p_{\text{diff}}(\psi)\right]\right\} \tag{8}$$

Several assumptions have been made in order to simplify the calculation. The diffuse phase angle function $p_{\text{diff}}(\psi)$ in Equation (8) assumes that the objects are spherical and that the reflectance is a constant for all wavelengths. This implies that the reflectance is gray body reflectance. Due to the complex nature of specular reflectance for manufactured space objects, it is assumed to be zero for the simulations. The addition of the specular component to the calculations contributes to higher visual magnitudes, thus by removing it the results of these simulations represent the lower bound on the visual magnitude of a particular object. A mean value of albedo for space debris has recently been estimated as 0.175 [13]; this value was used in the simulations for a_{diff}. Since the object catalog does not contain specific information regarding space object size, the diameter during a simulation was set to a constant value. A conservative lower bound on the detectable objects can be determined by setting the object diameter to 10 cm. The celestial sphere visualization does not show any information on the range and how the observer is constrained in terms of range to target. However, the range is tied directly to the detectability of an object through the visual magnitude calculation. By manipulation of the visual magnitude equation to solve for ρ, a region can be defined in which a chosen value of visible magnitude is guaranteed. Setting the limiting magnitude of the optics (m_{lim}), object reflectance, and the object size, the range can be calculated over the full range of solar phase angles. The result, Equation (9) is a constraint which presents the lower bound on the ranges at which object can be detected by a given optical sensor.

$$\rho = \|\mathbf{v}\| \leq \sqrt{\frac{d^2[a_{\text{spec}}/4 + a_{\text{diff}}\, p_{\text{diff}}(\psi)]}{10^{(m_{\text{sun}}-m_{\text{lim}})/2.5}}} \tag{9}$$

For generating an upper bound on detectable objects, a different form of the magnitude equation was considered. A conservative maximum bound on the quantity of light reflected by the SO towards the observer is made with the relative geometry of a simple flat plate. The plate is a model of a SO with conservatively large area A is shown in Figure 2. The apparent visible magnitude m_v sensed by an optical sensor may be written as

$$m_v = m_{\text{sun}} - 2.5\log_{10}\left[\frac{A}{\rho^2}\left\langle\hat{\mathbf{s}}\cdot\hat{\mathbf{n}}\right\rangle\left\langle\hat{\mathbf{v}}\cdot\hat{\mathbf{n}}\right\rangle\right] \tag{10}$$

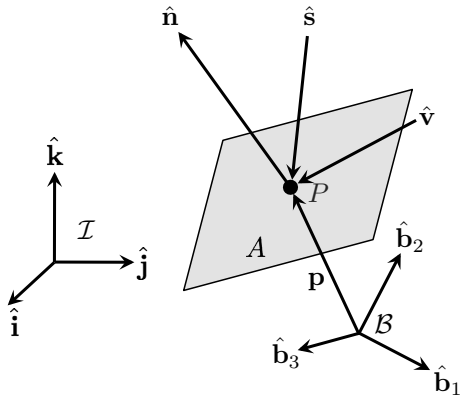

Figure 2. Flat plate reflection geometry

where ρ is the range from the object to the observer, A is the area of a perfectly reflective flat plate, $\hat{\mathbf{n}}$ is the normal vector of the plate in inertial coordinates, and the non-negative operator $\langle\cdot\rangle$ is defined as

$$\langle \xi \rangle = \begin{cases} \xi & \text{if} \quad \xi \geq 0 \\ 0 & \text{if} \quad \xi < 0 \end{cases} \tag{11}$$

One characteristic of optical sensors is a limiting magnitude m_{lim}, above which objects are too dim to be detected even with infinite integration time. Thus, the sensor-based apparent visible magnitude constraint that must be satisfied for a detection to be made is

$$m_{\text{sun}} - 2.5 \log_{10} \left[\frac{A}{\rho^2} \langle \hat{\mathbf{s}} \cdot \hat{\mathbf{n}} \rangle \langle \hat{\mathbf{v}} \cdot \hat{\mathbf{n}} \rangle \right] - m_{lim} \leq 0 \tag{12}$$

To ensure that the detection range is conservative, it is assumed that the target object is oriented perfectly such that the maximum quantity of photons are reflected to the observer. When this is the case, the surface normal $\hat{\mathbf{n}}$ represents a perfectly specular reflection as shown in Figure 3.

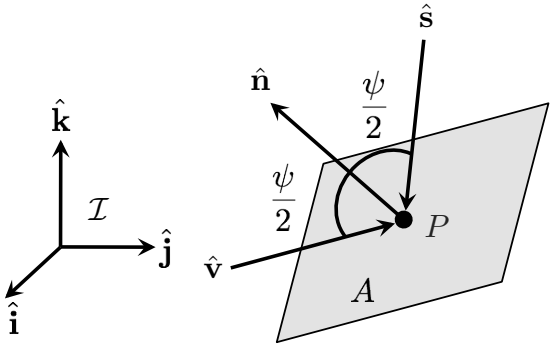

Figure 3. Surface normal geometry

$$\hat{\mathbf{n}} = \frac{\hat{\mathbf{v}} + \hat{\mathbf{s}}}{\|\hat{\mathbf{v}} + \hat{\mathbf{s}}\|} \tag{13}$$

Then,

$$\langle \hat{\mathbf{s}} \cdot \hat{\mathbf{n}} \rangle \langle \hat{\mathbf{v}} \cdot \hat{\mathbf{n}} \rangle = \left\langle \hat{\mathbf{s}} \cdot \frac{\hat{\mathbf{v}} + \hat{\mathbf{s}}}{\|\hat{\mathbf{v}} + \hat{\mathbf{s}}\|} \right\rangle \left\langle \hat{\mathbf{v}} \cdot \frac{\hat{\mathbf{v}} + \hat{\mathbf{s}}}{\|\hat{\mathbf{v}} + \hat{\mathbf{s}}\|} \right\rangle \tag{14}$$

$$= \left\langle \frac{\|\hat{\mathbf{s}}\|^2}{\|\hat{\mathbf{v}} + \hat{\mathbf{s}}\|} + \frac{\hat{\mathbf{s}} \cdot \hat{\mathbf{v}}}{\|\hat{\mathbf{v}} + \hat{\mathbf{s}}\|} \right\rangle \left\langle \frac{\|\hat{\mathbf{v}}\|^2}{\|\hat{\mathbf{v}} + \hat{\mathbf{s}}\|} + \frac{\hat{\mathbf{v}} \cdot \hat{\mathbf{s}}}{\|\hat{\mathbf{v}} + \hat{\mathbf{s}}\|} \right\rangle \tag{15}$$

$$= \frac{1}{\|\hat{\mathbf{v}} + \hat{\mathbf{s}}\|^2} \langle 1 + \hat{\mathbf{s}} \cdot \hat{\mathbf{v}} \rangle \langle 1 + \hat{\mathbf{v}} \cdot \hat{\mathbf{s}} \rangle \tag{16}$$

$$= \frac{1}{\|\hat{\mathbf{v}}\|^2 + \|\hat{\mathbf{s}}\|^2 + 2\hat{\mathbf{s}} \cdot \hat{\mathbf{v}}} \langle 1 + \hat{\mathbf{s}} \cdot \hat{\mathbf{v}} \rangle \langle 1 + \hat{\mathbf{v}} \cdot \hat{\mathbf{s}} \rangle \tag{17}$$

$$= \frac{1 + 2\hat{\mathbf{s}} \cdot \hat{\mathbf{v}} + \|\hat{\mathbf{s}} \cdot \hat{\mathbf{v}}\|^2}{2 + 2\hat{\mathbf{s}} \cdot \hat{\mathbf{v}}} \tag{18}$$

$$= \frac{(1 + \hat{\mathbf{s}} \cdot \hat{\mathbf{v}})^2}{2\,(1 + \hat{\mathbf{s}} \cdot \hat{\mathbf{v}})} \tag{19}$$

$$= \frac{1}{2}\,(1 + \hat{\mathbf{s}} \cdot \hat{\mathbf{v}}) \tag{20}$$

Because the angle between $\hat{\mathbf{s}}$ and $\hat{\mathbf{v}}$ is ψ, the solar phase angle, then $\hat{\mathbf{s}} \cdot \hat{\mathbf{v}} = \cos\psi$, and the above expression reduces further

$$\langle \hat{\mathbf{s}} \cdot \hat{\mathbf{n}} \rangle \langle \hat{\mathbf{v}} \cdot \hat{\mathbf{n}} \rangle = \frac{1 + \cos\psi}{2} \tag{21}$$

When the solar phase angle $\psi \to 0$, the observer senses a reflective area of A (the maximum possible). Conversely, as $\phi \to \pi$, the sensed reflective area approaches zero. Given a conservative bound on the perfectly reflecting SO area A, the detectability constraint may then be written in terms of range ρ as

$$m_{\text{sun}} - 2.5 \log_{10} \left[\frac{A}{\rho^2} \frac{1 + \cos\psi}{2} \right] \leq m_{lim} \tag{22}$$

$$\frac{2}{5}\,(m_{\text{sun}} - m_{lim}) \leq \log_{10} \left[\frac{A}{\rho^2} \frac{1 + \cos\psi}{2} \right] \tag{23}$$

$$10^{2/5(m_{\text{sun}} - m_{lim})} \leq \frac{A}{\rho^2} \frac{(1 + \cos\psi)}{2} \tag{24}$$

$$\rho^2 \leq \frac{A(1 + \cos\psi)}{2 \cdot 10^{2/5(m_{\text{sun}} - m_{lim})}} \tag{25}$$

Because only $\rho > 0$ are physical solutions, only the positive root is of interest, so the upper bound range constraint constraint may be written as

$$\rho \leq \sqrt{\frac{A(1 + \cos\psi)}{10^{2/5(m_{\text{sun}} - m_{lim})}}} = \sqrt{\frac{A(1 + \hat{\mathbf{s}} \cdot \hat{\mathbf{v}})}{10^{2/5(m_{\text{sun}} - m_{lim})}}} \tag{26}$$

Unlike Equation (9), the above range is independent of the albedo of the object. By considering perfectly specular reflectance, an upper bound is defined on the range at which a particular magnitude object can be detected.

It should be noted that the visual magnitude of the object does not alone indicate the sensor's ability to see the target object. For instance, a ground based observation of an object during daytime will not result in the sensor detecting the object, even if the object apparent magnitude is better than the limiting magnitude of the optics. Space based sensors do not have this problem. In general, for observations made in visible wavelengths the atmosphere is opaque during daytime.

Objects within Sensor FOV

The consideration of LOS, illumination, and magnitude establish the detectability for all of the objects in the catalog. In order to determine which objects are actually visible for a given observer, the observer's field-of-view (FOV), pointing direction, and limiting magnitude must also be known. Given a pointing direction $\hat{\mathbf{p}}$ and a size of the field of view for a specific sensor, the object was marked as either in view or out of view by determining the projected angles between the center of the field of view, as indicated by the pointing direction $\hat{\mathbf{p}}$, and the direction to the object $\hat{\mathbf{v}}$. To define the FOV region, a roll angle ϕ is defined to represent the rotation of the field of view about $\hat{\mathbf{p}}$.

$$\left[\arctan\left(\frac{\hat{p}_y}{\hat{p}_x}\right) - \frac{FOV}{2}\right]\cos\phi + \left[\arcsin(\hat{p}_z) - \frac{FOV}{2}\right]\sin\phi \leq \arctan\left(\frac{\hat{v}_y}{\hat{v}_x}\right) \tag{27}$$

$$\left[\arctan\left(\frac{\hat{p}_y}{\hat{p}_x}\right) + \frac{FOV}{2}\right]\cos\phi + \left[\arcsin(\hat{p}_z) - \frac{FOV}{2}\right]\sin\phi \leq \arctan\left(\frac{\hat{v}_y}{\hat{v}_x}\right) \tag{28}$$

$$\left[\arctan\left(\frac{\hat{p}_y}{\hat{p}_x}\right) - \frac{FOV}{2}\right](-\sin\phi) + \left[\arcsin(\hat{p}_z) - \frac{FOV}{2}\right]\cos\phi \leq \arcsin(\hat{v}_z) \tag{29}$$

$$\left[\arctan\left(\frac{\hat{p}_y}{\hat{p}_x}\right) - \frac{FOV}{2}\right](-\sin\phi) + \left[\arcsin(\hat{p}_z) + \frac{FOV}{2}\right]\cos\phi \geq \arcsin(\hat{v}_z) \tag{30}$$

These four conditions must be satisfied in order for an object to be within the sensor's field of view. The equations define the boundaries of the FOV, thus any object meeting all four conditions are within FOV of the observer.

3D Visualization of Constraints

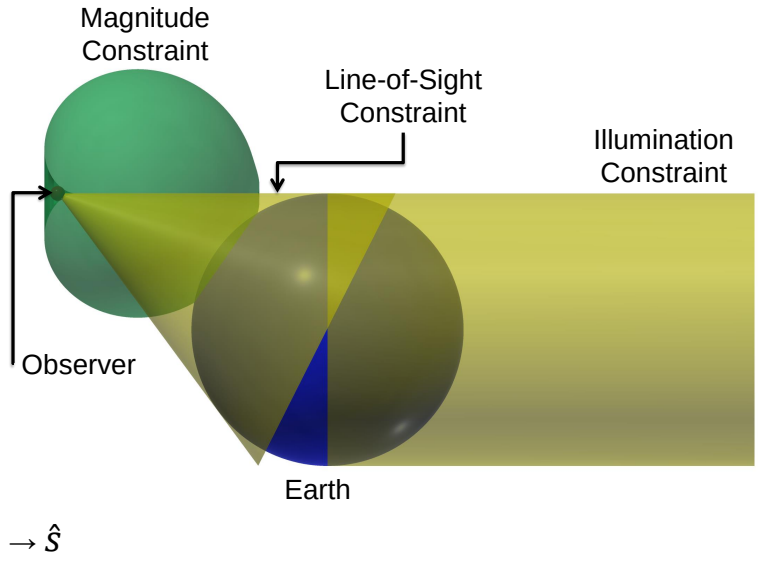

Figure 4. Illustration of the constraint surfaces in 3D

The equations presented for determining detectability contribute to defining surfaces which shows the limits of detectability for the observer. Combining the previously defined constraints defined for

illumination and line of sight, a 3D visualization of the region in which objects are visible can be determined based on a value of minimum visual magnitude and some given diameter. Figure 4 shows the constraints for 10 cm objects with magnitudes lower than 15. The Earth is represented as a blue sphere and the LOS constraint is the cone extending from the observer to the Earth. The illumination constraint is a cylinder extending from the Earth in the direction of the sun vector. The magnitude constraint takes the shape defined by Equation (9). The volume enclosed by the magnitude constraint that lies outside of the LOS and illumination surfaces is the region where the observer can detect objects.

ADMISSIBLE REGION

Looking again a Figure (4), a dependence on range can be seen for all of the constraints. Through manipulating this range dependence, these constraints can be imposed on the possible range space objects are from the observer. When considering the capabilities of a space based optical sensor like the ones being considered for RECONSO, typically the bearing and bearing rates are captured by the sensor and additional methods are required in order to determine the full state of a space object. By combining these constraint and admissible regions for space-based optical observations of Earth-orbiting objects [9], smaller admissible regions can be determined for a given observation which can assist in the initial orbit determination of space objects.

A common approach to defining and computing an admissible region for the range ρ and range rate $\dot{\rho}$ is briefly introduced. The observer makes bearing measurements of right ascension α and declination δ of an object from an observation location defined as $\mathbf{o}$. If multiple measurements are taken over a short period of time, the apparent angular rates of the bearing measurements $\dot{\alpha}$ and $\dot{\delta}$ can be approximated. With the bearings and bearing rates, the attributable vector can be defined as $\mathcal{A} = (\alpha, \delta, \dot{\alpha}, \dot{\delta})$. It is assumed in the following calculations that $\mathcal{A}$ is known by the observer. The inertial position $\mathbf{r}$ of a space object (SO) may be expressed in terms of an observer position $\mathbf{o}$ and the line-of-sight vector $\mathbf{v}$ as

$$\mathbf{r} = \mathbf{o} + \mathbf{v} \tag{31}$$

The geometry of the space object, observer, line of sight vector, sun vector $\mathbf{s}$, and the inertial frame $\mathcal{I} : \{\hat{\mathbf{i}}, \hat{\mathbf{j}}, \hat{\mathbf{k}}\}$ are described in Figure 5. The measurements taken by the observer only include the inertial bearings of the SO; however, the geometry allows the line of sight vector to be defined in terms of range and the inertial bearings by

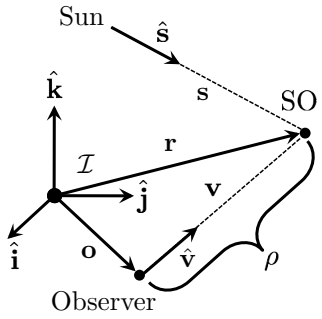

Figure 5. Observer Geometry

$$\mathbf{v} = \rho\hat{\mathbf{v}} = \rho \begin{bmatrix} \cos\alpha\cos\delta \\ \sin\alpha\cos\delta \\ \sin\alpha \end{bmatrix} \tag{32}$$

where ρ is the unknown range to the object from the observer to the SO. Likewise, the velocity of the SO $\dot{\mathbf{r}}$ is computed as

$$\frac{\mathrm{d}}{\mathrm{d}t}\mathbf{r} = \dot{\mathbf{r}} = \frac{\mathrm{d}\mathbf{o}}{\mathrm{d}t} + \frac{\mathrm{d}\rho}{\mathrm{d}t}\hat{\mathbf{v}} + \rho\frac{\partial\hat{\mathbf{v}}}{\partial\alpha}\frac{\mathrm{d}\alpha}{\mathrm{d}t} + \rho\frac{\partial\hat{\mathbf{v}}}{\partial\delta}\frac{\mathrm{d}\delta}{\mathrm{d}t} \tag{33}$$

which is simplified as

$$\dot{\mathbf{r}} = \dot{\mathbf{o}} + \dot{\rho}\hat{\mathbf{v}} + \rho\hat{\mathbf{v}}_\alpha\dot{\alpha} + \rho\hat{\mathbf{v}}_\delta\dot{\delta} \tag{34}$$

Eq. (34) introduces the remaining unknown state parameter, the range-rate $\dot{\rho}$. Combined with the attributable vector $\mathcal{A} = (\alpha, \delta, \dot{\alpha}, \dot{\delta})$, $(\rho, \dot{\rho})$ are sufficient to fully calculate the instantaneous Cartesian state of the SO using (31) and (34). As of yet, the only constraint on $(\rho, \dot{\rho})$ is that $\rho > 0$. In order to further constrain the problem, other constraints may be added based on physical limitations. For SOs in closed sustainable orbits about Earth, there are several constraints that can be imposed on $\mathbf{r}$ and $\dot{\mathbf{r}}$ (and thus on $(\rho, \dot{\rho})$:

Common Admissible Region Constraints

It is common for admissible regions to be constrained by the specific orbital energy for sustainable Earth orbits [14, 15, 16]. For a closed orbit about the Earth, the orbit must not be parabolic or hyperbolic. Thus, the mass-specific orbital energy about Earth (ε) must satisfy the constraint

$$\varepsilon(\rho, \dot{\rho}) = \frac{\dot{\mathbf{r}}(\rho, \dot{\rho}) \cdot \dot{\mathbf{r}}(\rho, \dot{\rho})}{2} - \frac{\mu}{\sqrt{\mathbf{r}(\rho) \cdot \mathbf{r}(\rho)}} \leq 0 \tag{35}$$

where $\mathbf{r}(\rho)$ and $\dot{\mathbf{r}}(\rho, \dot{\rho})$ correspond to (31) and (34), respectively.

A sustainable orbit does not decay rapidly due to atmospheric drag or impact the Earth. Thus the periapsis of an orbit must be above the surface of the Earth at the very least, or above the atmosphere in order to be sustainable [10]. Considering this limit on periapsis, a constraint can be imposed as

$$r_p(\rho, \dot{\rho}) = a(\rho, \dot{\rho})(1 - e(\rho, \dot{\rho})) = -\frac{1}{2\varepsilon(\rho, \dot{\rho})}(1 - e(\rho, \dot{\rho})) \geq R_e + h_{\mathrm{atm}} \tag{36}$$

There is also a more general constraint that the semi-major axis $a(\rho, \dot{\rho}) >= R_e + h_{\mathrm{atm}}$, yielding

$$\varepsilon(\rho, \dot{\rho}) \geq \varepsilon_{\min} = -\frac{1}{2(R_e + h_{\mathrm{atm}})} \tag{37}$$

Illuminated Space Objects

Since objects which are eclipsed by the Earth cannot be seen by an observer, the illumination constraint can be applied to admissible regions through its dependence on ρ. For an object to be in shadow, it must meet the inequalities defined in Equations (4) and (5). Considering the relationship presented in (31),

$$\hat{\mathbf{s}} \cdot (\mathbf{o} + \rho\hat{\mathbf{v}}) \geq 0 \tag{38}$$

$$\hat{\mathbf{s}} \times (\mathbf{o} + \rho\hat{\mathbf{v}}) \leq R_e \tag{39}$$

Rearranging Equation (38) yields

$$\rho \geq -\frac{\mathbf{o} \cdot \hat{\mathbf{s}}}{\hat{\mathbf{v}} \cdot \hat{\mathbf{s}}} \tag{40}$$

Expanded, Equation (39) can be rewritten as

$$[\hat{\mathbf{s}} \times \mathbf{o} + \rho \hat{\mathbf{s}} \times \hat{\mathbf{v}}] \cdot [\hat{\mathbf{s}} \times \mathbf{o} + \rho \hat{\mathbf{s}} \times \hat{\mathbf{v}}] \leq R_e^2 \tag{41}$$

Further manipulation yields the following quadratic inequality in ρ

$$\rho^2 \|\hat{\mathbf{s}} \times \hat{\mathbf{v}}\|^2 + 2\rho \left(\hat{\mathbf{s}} \times \hat{\mathbf{v}}\right) \cdot \left(\hat{\mathbf{s}} \times \mathbf{o}\right) + \|\hat{\mathbf{r}} \times \hat{\mathbf{v}}\|^2 - R_e^2 \leq 0 \tag{42}$$

However, the SO is shadowed by the Earth when this constraint is satisfied, so it is illuminated when the inequality is reversed:

$$\rho^2 \|\hat{\mathbf{s}} \times \hat{\mathbf{v}}\|^2 + 2\rho \left(\hat{\mathbf{s}} \times \hat{\mathbf{v}}\right) \cdot \left(\hat{\mathbf{s}} \times \mathbf{o}\right) + \|\hat{\mathbf{r}} \times \hat{\mathbf{v}}\|^2 - R_e^2 \geq 0 \tag{43}$$

The roots of the quadratic inequality in Equation (43) are of interest because they denote eclipse transition points. The ranges of these eclipse transitions denote regions where objects are eclipsed and where they are not. Four possible solutions exist for this inequality. Case 1, the solution is complex, implying that no eclipse conditions exist at any point along $\mathbf{v}$. Case 2 is non-physical as range cannot be a negative number. Case 3 is a valid solution, however in this range the space object is on the sun-facing side of the Earth. Case 4 is the solution which shows where eclipse transitions occur.

$$\begin{aligned}
&\text{Case 1: } \rho_1, \rho_2 \in \mathbb{C} \\
&\text{Case 2: } \rho_1 \text{ and/or } \rho_2 \leq 0 \\
&\text{Case 3: } 0 < \rho_1, \rho_2 < -\frac{\mathbf{o} \cdot \hat{\mathbf{s}}}{\hat{\mathbf{v}} \cdot \hat{\mathbf{s}}} \\
&\text{Case 4: } \rho_1, \rho_2 < -\frac{\mathbf{o} \cdot \hat{\mathbf{s}}}{\hat{\mathbf{v}} \cdot \hat{\mathbf{s}}} \leq \rho_1 \text{ and/or } \rho_2
\end{aligned} \tag{44}$$

Inclination Constraint

In special situations where the bounding range of possible inclinations are known (such as in breakups, graveyard orbit objects, or HAMR debris), bounds in the admissible inclinations can substantially reduce the size of the admissible region, aiding initial orbit determination. It can be especially hazardous to unduly limit the ranges of admissible inclinations *a-priori*, as objects that are outside of these bounds (yet still observed) will generate neither real associations when compared with new data nor produce plausible initial orbits. Recall that orbit inclination $i \in [0, \pi]$ is defined as

$$\mathbf{h} \cdot \hat{\mathbf{k}} = \|\mathbf{h}\| \cos i \tag{45}$$

Suppose that limits $0 \leq i_l < i_u \leq \pi$ are chosen over some range of ρ. Then, (45) requires that admissible $(\rho, \dot{\rho})$ regions satisfy

$$\cos i_l \geq \frac{\mathbf{h}(\rho, \dot{\rho}) \cdot \hat{\mathbf{k}}}{\|\mathbf{h}(\rho, \dot{\rho})\|} \geq \cos i_u \tag{46}$$

The present form of the constraint is difficult to solve. To move forward, all sides of the equation are multiplied by $\|\mathbf{h}(\rho, \dot{\rho})\|$ and squared, producing the following piecewise-defined inequalities for

the lower limit i_l and upper limit i_u:

$$\begin{cases} \mathbf{h}(\rho,\dot\rho)\cdot\mathbf{h}(\rho,\dot\rho)\cos^2 i_l \le \mathbf{h}(\rho,\dot\rho)\cdot\hat{\mathbf{k}} & \text{if} \quad 0 \le i_l \le \frac{\pi}{2} \\ -\mathbf{h}(\rho,\dot\rho)\cdot\mathbf{h}(\rho,\dot\rho)\cos^2 i_l \ge \mathbf{h}(\rho,\dot\rho)\cdot\hat{\mathbf{k}} & \text{if} \quad \frac{\pi}{2} < i_l \le \pi \\ \mathbf{h}(\rho,\dot\rho)\cdot\mathbf{h}(\rho,\dot\rho)\cos^2 i_l \ge \mathbf{h}(\rho,\dot\rho)\cdot\hat{\mathbf{k}} & \text{if} \quad 0 \le i_u \le \frac{\pi}{2} \\ -\mathbf{h}(\rho,\dot\rho)\cdot\mathbf{h}(\rho,\dot\rho)\cos^2 i_l \le \mathbf{h}(\rho,\dot\rho)\cdot\hat{\mathbf{k}} & \text{if} \quad \frac{\pi}{2} < i_u \le \pi \end{cases} \tag{47}$$

Using (31) and (34), the mass-specific angular momentum of the SO is

$$\mathbf{h} = \mathbf{r}(\rho)\times\dot{\mathbf{r}}(\rho,\dot\rho) \tag{48}$$

which after expansion gives

$$\mathbf{h}(\rho,\dot\rho) = \rho^2\hat{\mathbf{v}}\times\left(\dot\alpha\hat{\mathbf{v}}_\alpha + \dot\delta\hat{\mathbf{v}}_\delta\right) + \rho\left[\mathbf{o}\times\left(\dot\alpha\hat{\mathbf{v}}_\alpha + \dot\delta\hat{\mathbf{v}}_\delta\right) + \hat{\mathbf{v}}\times\dot{\mathbf{o}}\right] + \mathbf{o}\times\dot{\mathbf{o}} + \dot\rho\mathbf{o}\times\hat{\mathbf{v}} \tag{49}$$

Using the definitions

$$\mathbf{h}_3 = \hat{\mathbf{v}}\times\left(\dot\alpha\hat{\mathbf{v}}_\alpha + \dot\delta\hat{\mathbf{v}}_\delta\right) \tag{50}$$

$$\mathbf{h}_2 = \mathbf{o}\times\left(\dot\alpha\hat{\mathbf{v}}_\alpha + \dot\delta\hat{\mathbf{v}}_\delta\right) + \hat{\mathbf{v}}\times\dot{\mathbf{o}} \tag{51}$$

$$\mathbf{h}_1 = \mathbf{o}\times\dot{\mathbf{o}} \tag{52}$$

$$\mathbf{h}_0 = \mathbf{o}\times\hat{\mathbf{v}} \tag{53}$$

The relation (49) may be written more simply as

$$\mathbf{h}(\rho,\dot\rho) = \rho^2\mathbf{h}_3 + \rho\mathbf{h}_2 + \mathbf{h}_1 + \dot\rho\mathbf{h}_0 \tag{54}$$

The expression $\mathbf{h}(\rho,\dot\rho)\cdot\hat{\mathbf{k}}$ is similarly written as

$$\mathbf{h}(\rho,\dot\rho)\cdot\hat{\mathbf{k}} = \rho^2\mathbf{h}_3\cdot\hat{\mathbf{k}} + \rho\mathbf{h}_2\cdot\hat{\mathbf{k}} + \mathbf{h}_1\cdot\hat{\mathbf{k}} + \dot\rho\mathbf{h}_0\cdot\hat{\mathbf{k}} = \rho^2 k_3 + \rho k_2 + k_1 + \dot\rho k_0 \tag{55}$$

while $\mathbf{h}(\rho,\dot\rho)\cdot\mathbf{h}(\rho,\dot\rho)\cos^2 i_l$ becomes

$$\begin{aligned}\mathbf{h}(\rho,\dot\rho)\cdot\mathbf{h}(\rho,\dot\rho)\cos^2 i_l = {}& \dot\rho^2\mathbf{h}_0\cdot\mathbf{h}_0\cos^2 i_l + \dot\rho\left(\rho^2 2\mathbf{h}_0\cdot\mathbf{h}_3 + \rho 2\mathbf{h}_0\cdot\mathbf{h}_2 + 2\mathbf{h}_0\cdot\mathbf{h}_1\right)\cos^2 i_l \\ & + \left[\rho^4\mathbf{h}_3\cdot\mathbf{h}_3 + \rho^3 2\mathbf{h}_2\cdot\mathbf{h}_3 + \rho^2\left(\mathbf{h}_2\cdot\mathbf{h}_2 + 2\mathbf{h}_1\cdot\mathbf{h}_3\right) + \rho 2\mathbf{h}_1\cdot\mathbf{h}_2 + \mathbf{h}_1\cdot\mathbf{h}_1\right]\end{aligned} \tag{56}$$

For notational convenience, the following definitions are made:

$$s_2 = \mathbf{h}_0\cdot\mathbf{h}_0\cos^2 i_l \tag{57}$$

$$s_1(\rho) = \left(\rho^2 2\mathbf{h}_0\cdot\mathbf{h}_3 + \rho 2\mathbf{h}_0\cdot\mathbf{h}_2 + 2\mathbf{h}_0\cdot\mathbf{h}_1\right)\cos^2 i_l \tag{58}$$

$$s_0(\rho) = \left[\rho^4\mathbf{h}_3\cdot\mathbf{h}_3 + \rho^3 2\mathbf{h}_2\cdot\mathbf{h}_3 + \rho^2\left(\mathbf{h}_2\cdot\mathbf{h}_2 + 2\mathbf{h}_1\cdot\mathbf{h}_3\right) + \rho 2\mathbf{h}_1\cdot\mathbf{h}_2 + \mathbf{h}_1\cdot\mathbf{h}_1\right]\cos^2 i_l \tag{59}$$

The inclination inequality constraint then becomes

$$\mathbf{h}(\rho,\dot\rho)\cdot\mathbf{h}(\rho,\dot\rho)\cos^2 i_l = \dot\rho^2 s_2 + \dot\rho s_1(\rho) + s_0(\rho) \ge \rho^2 k_3 + \rho k_2 + k_1 + \dot\rho k_0 = \mathbf{h}(\rho,\dot\rho)\cdot\hat{\mathbf{k}} \tag{60}$$

Enumerating all cases for the upper and lower inclination limits produces

$$\begin{cases} \dot\rho^2 s_2 + \dot\rho\left(s_1(\rho) - k_0\right) + \left(-\rho^2 k_3 - \rho k_2 - k_1 + s_0(\rho)\right) \le 0 & \text{if} \quad 0 \le i_l \le \frac{\pi}{2} \\ \dot\rho^2 s_2 + \dot\rho\left(s_1(\rho) + k_0\right) + \left(\rho^2 k_3 + \rho k_2 + k_1 + s_0(\rho)\right) \le 0 & \text{if} \quad \frac{\pi}{2} < i_l \le \pi \\ \dot\rho^2 s_2 + \dot\rho\left(s_1(\rho) - k_0\right) + \left(-\rho^2 k_3 - \rho k_2 - k_1 + s_0(\rho)\right) \ge 0 & \text{if} \quad 0 \le i_u \le \frac{\pi}{2} \\ \dot\rho^2 s_2 + \dot\rho\left(s_1(\rho) + k_0\right) + \left(\rho^2 k_3 + \rho k_2 + k_1 + s_0(\rho)\right) \ge 0 & \text{if} \quad \frac{\pi}{2} < i_u \le \pi \end{cases} \tag{61}$$

THE SIMULATION

A simulation is presented which is capable of representing the cataloged space debris environment as encountered by the observer. The utility of the simulation is in its application of the constraints presented, which determine detectability for each object in the catalog. The current catalog is used as an approximation of the space debris environment, providing valuable information on where new detections can be made. The current publicly available space object catalog from Space-Track contains 14,108 unclassified objects. These objects are defined using classical orbital elements in a Two-Line-Element (TLE) file. This format organizes the information describing the orbits of each object at the epoch of the observation. Each set of two lines has orbital elements which can be used with simple perturbation models to define the ECI state of the object. One of the standard simple perturbation models is SGP4 [17]. These models are widely used with TLE datasets, and the propagation codes for these models are readily available in a variety of programming languages [18]. The simulation algorithm was written based on the SGP4 propagation. For a satellite observer, the orbit was defined in TLE format, then, using MATLAB's version of the SGP4 propagation algorithm, the ECI position and velocity for each of the objects in the catalog's TLE file and the observer TLE file were calculated over a period of time. The SGP4 algorithm used minutes from epoch as its time unit. Definition of time period of propagation included the minutes from epoch at the start, minutes from epoch at the end of the time period, and the step size. The epoch at which the individual observations of objects in the catalog were made can differ by several days, and can differ vastly from the date desired for the simulation. In order to address this, the simulation date has to be known and the duration in minutes has to be known before propagation. Each object's starting minutes from epoch value is then calculated such that every object starts at the date desired for the simulation. Ephemeris data provided by JPL was used in addition to generate the ECI positions of the Moon and the Sun [19]. Since the purpose of these simulations was to aid in estimating ideal pointing and probability of detection, the 3D ECI data was transformed into celestial sphere data with axes of right ascension and declination. This transformation was performed using Equations (62) and (63), converting the unit vector $\hat{\mathbf{v}}$ into right ascension, α, and declination, δ.

$$\alpha = \arctan\left(\frac{\hat{v}_y}{\hat{v}_x}\right) \tag{62}$$

$$\delta = \arcsin(\hat{v}_z) \tag{63}$$

Because the simulation is concerned with identifying visible objects with respect to an observer, α and δ, are computed as seen by the observer. Rather than having the Earth as the center of the coordinate system, the position of the observer was chosen as the center. This implied that the projection of the latitude and longitude data would show the 4π steradian view from the observer's prospective. To achieve this, the ECI coordinates of the observer were subtracted from each of the objects, the Sun, Moon, and Earth before being transformed into right ascension and declination data. The distance information was discarded as it was not needed for the celestial sphere projection. A hammer map projection of the celestial sphere provided a convenient visualization with minimal distortion [20]. The Earth, Moon, and Sun were mapped with radii in the angular space based on Equation (64) below, where D is the diameter and $\mathbf{v}_{\text{body}}$ is the observer-centered position of the body.

$$\text{Angular Radius} = \arctan\left(\frac{D}{2\|\mathbf{v}_{\text{body}}\|}\right) \tag{64}$$

The projection also includes exclusion zones for these bodies due to their brightness. The pointing of sensitive optics within some distance of these bodies could cause damage to the system or prevent objects from being detected. A zone equal to the size of the FOV of the sensor has been defined as the exclusion zone around the Earth, Moon, and Sun. These appear as semi-transparent extensions of the projected Earth, Moon, and Sun bodies. The pointing vector $\hat{\mathbf{p}}$ was defined as either a constant value, for inertially fixed pointing, or a time-varying quantity. The objects themselves were plotted as gray dots on the projection. In addition, a projection could be made for every time step of the analysis and saved to a video. The change in object location over time, such as the position of the Earth relative to the observer, could be easily viewed in a projection movie. Furthermore, general pointing trajectories could be formed by analyzing a simulation over a period of time and identifying regions of interest and noting the time at which to point there.

RESULTS

To demonstrate the simulation and the constraints presented, two observers are chosen: A RECONSO satellite observer at 700 km altitude, and a ground telescope placed at the South Pole. The results presented shows several visualizations from each observer's simulation. The results shown depict the quantity of objects and the location on the celestial sphere where objects may be detectable. In order to demonstrate the constraints on the admissible region, the four test cases described in Equation (44) were chosen to represent different observation scenarios. Visualizations of the four scenarios and their corresponding admissible regions are shown in this section, demonstrating the impacts on the admissible region.

Simulation Results

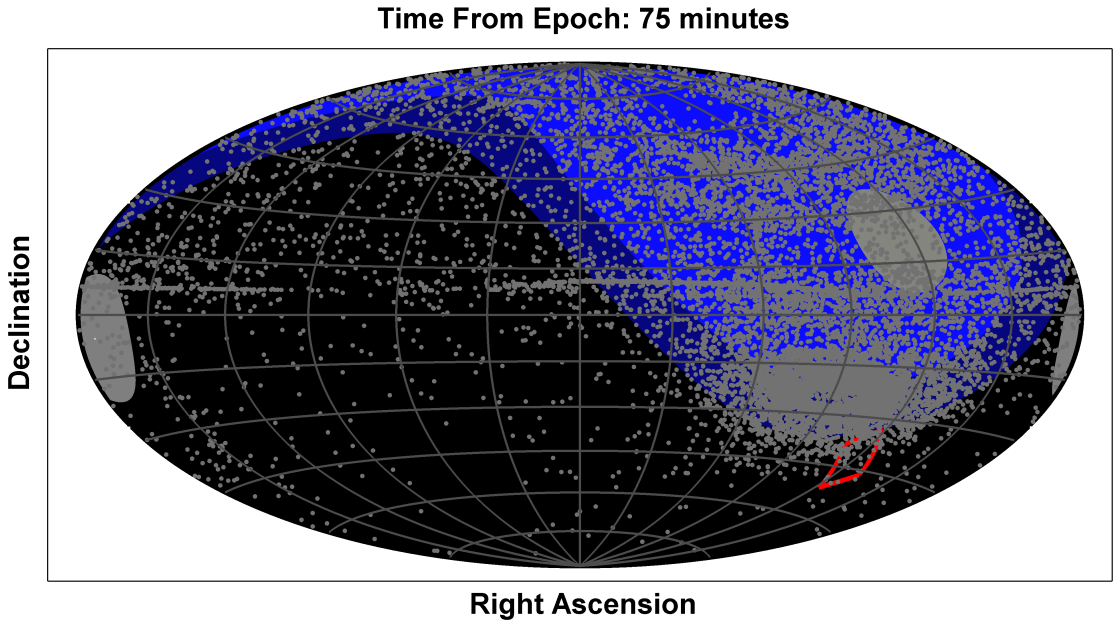

Figure 6. Simulation at 75 minutes from epoch

The observer was selected for simulation in LEO at an altitude of 700km. The optics were set to point 10° above the velocity vector with a 15° by 15° rectangular field of view. A frame from the

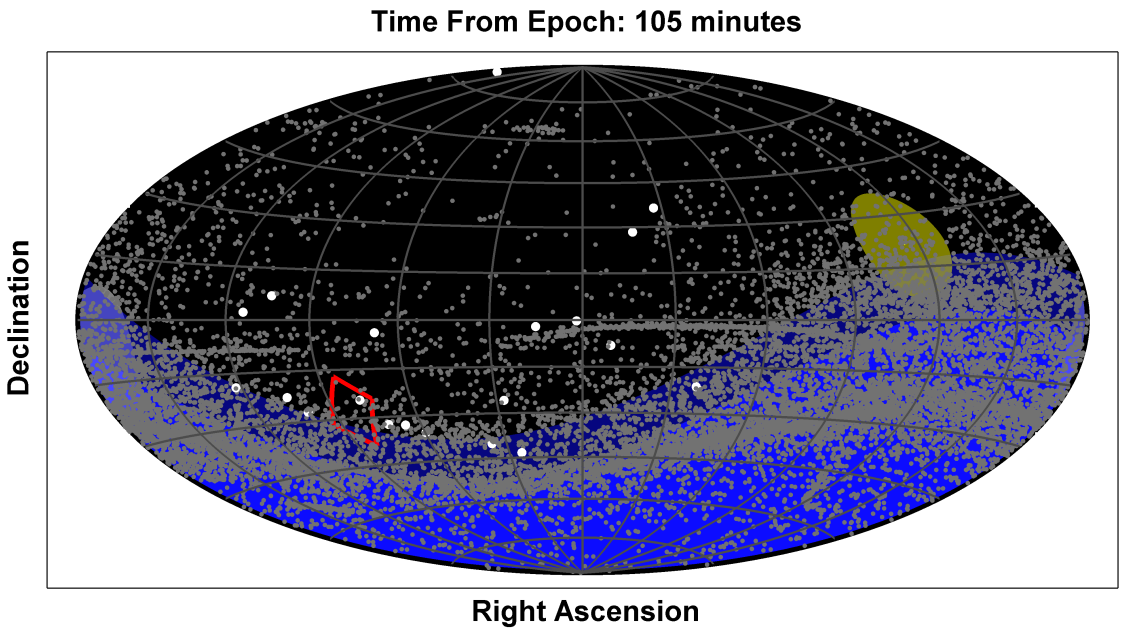

Figure 7. Simulation at 105 minutes from epoch

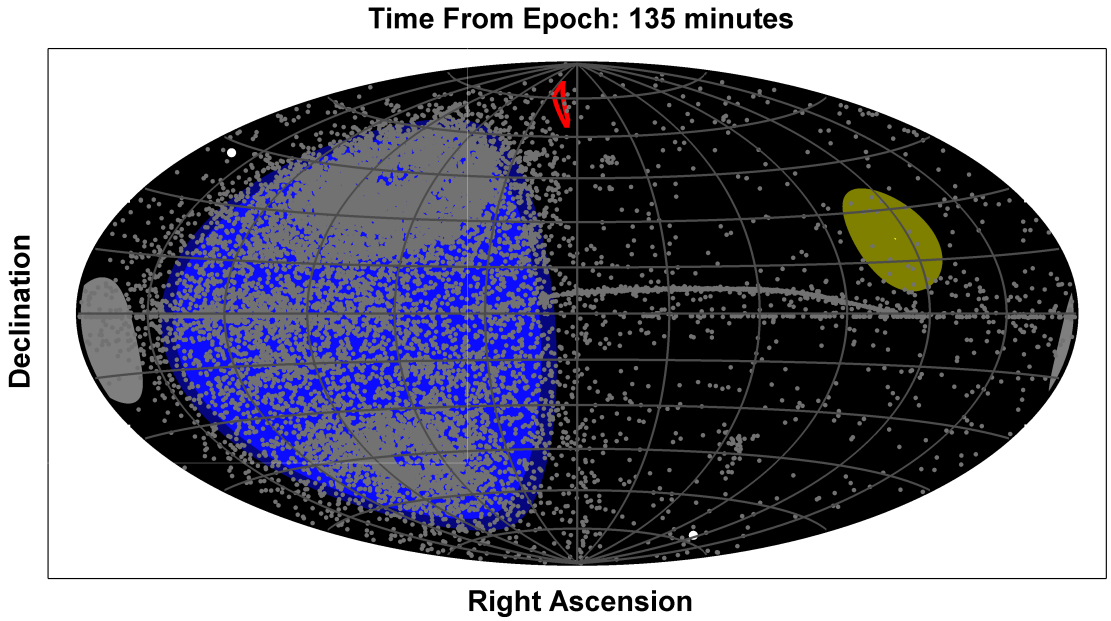

Figure 8. Simulation at 135 minutes from epoch

simulation is shown in Figure 6 at time $t = 75$ minutes from the epoch of midnight 15 July 2013. The limiting magnitude is set to 12, a conservative value that approximates the optical sensors considered for RECONSO. Several features of the space object environment surrounding Earth can be identified from the simulated image. The belt of objects near $\delta = 0^{\circ}$ is the geostationary belt, and the curved line of objects nearby is the graveyard orbit for defunct geostationary satellites. In

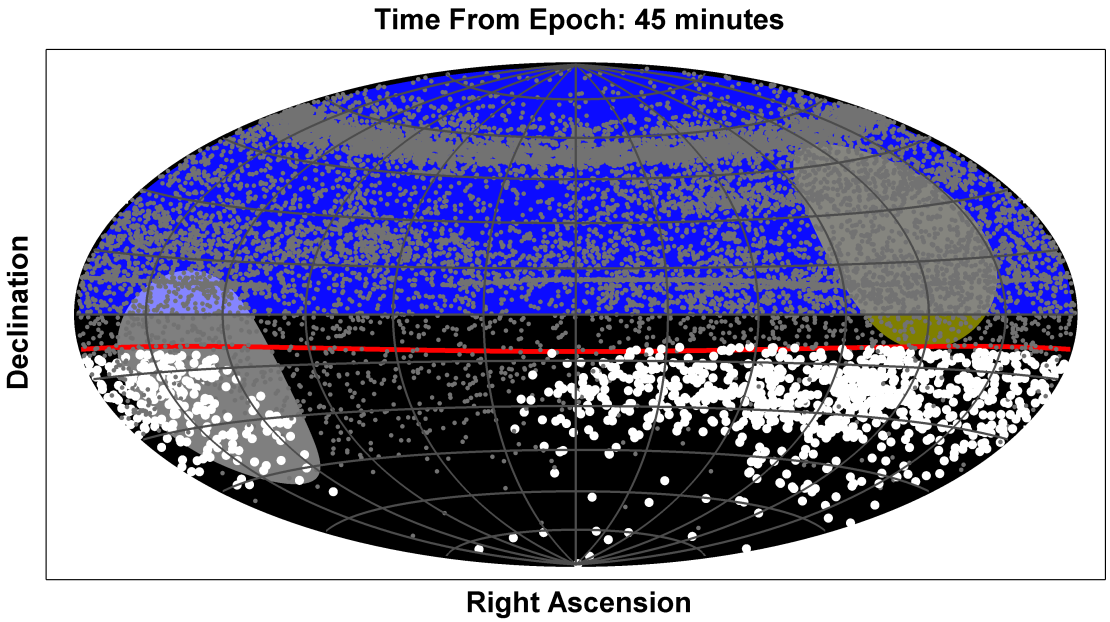

Figure 9. Simulation from ground telescope in Antartica

addition, there are high density regions of objects at either poles of the Earth. The field of view of the observer is outlined in red and any objects appearing white within this region are currently visible to the observer. Visibility being defined as an object meeting all the constraints listed in the Optical Detection of Objects section. The figures show the progression of the observer through its orbit at 75 minutes, 105 minutes, and 135 minutes from epoch. These images show three distinct states in the observer's orbit. At 75 minutes from epoch, the Earth and Sun are on the same side with respect to the observer. Furthermore, the field of view of the observer is now pointed into the region currently being eclipsed by the Earth. Stepping forwards 30 minutes later, objects are detectable because they are no longer eclipsed by the sun. In addition, 1 object is currently within the observer's field of view at this pointing direction. However it can be seen that if the pointing direction were to be changed, many more objects could be detected. At 135 minutes from epoch, the Earth is now on the opposite side of the sun with respect to the observer. Considering the illumination constraint, all objects projected within the radius of the Earth cannot be visible since they are currently eclipsed. Currently, the field of view has no objects within it that are detectable. In looking at simulation images such as these over time, it can be seen how an optimum pointing location can be defined either by inspection or with an algorithm which looks for the highest density of detectable objects over time and reports an optimum pointing trajectory as the output. Such a trajectory could then be used for the simulated observer in subsequent simulations to ensure the expected performance is provided. Figure 9 shows the projection from an observer placed at the South Pole with a limiting magnitude of 15. The limiting magnitude is higher for the telescope due to much larger and more capable optics compared with the RECONSO observer. The same detection constraints imposed for orbiting observers are relevant for ground observations as well.

By assessing each object's visibility throughout the course of the analysis, the number of objects visible to observer can be recorded. This information can then be used as a performance metric for determining how a pointing trajectory performs in terms of known object detection rates. If

the current catalog spatial distribution is a good approximation of the untracked object distribution, such trajectories can also generate larger quantities of newly detected objects. The plots shown in 10 show the number of objects both detectable and undetectable in the field of view of the observer over a period of 270 minutes, which corresponds to approximately 3 orbits of the observer satellite.

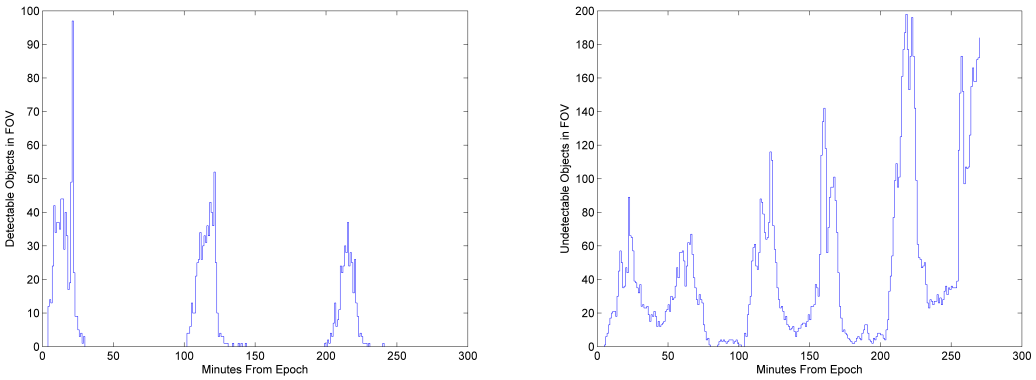

Figure 10. Detectable (left) and Undetectable (right) objects in FOV

Example Admissible Regions

To visualize the proposed admissible region constraints, several test cases and their corresponding admissible regions are shown. The parameters chosen for the example cases are shown in Table 1. All cases described in Table 1 use canonical units, with 1 DU= R_e, 1 TU=$\sqrt{\mu/R_e}$, and $\mu = 1$ DU^2/TU^3. The first case, shown in Figure 11, considers a line of sight vector between the observer and the object that is not eclipsed by the Earth. As such, there is no additional constraints imposed on the admissible region plot shown to the right of the case geometry. Case 2 considers the observer to be on the Earth's surface in eclipse, which implies the line of sight vector is in eclipse for some distance near the observer. The is represented in the admissible region plot as the vertical line near $\rho = 2$. This line, a solution to the quadratic in Equation (43), shows the range at which the eclipsed portion of the line of sight vector transitions to being sun lit, imposing a constraint on the admissible region. Likewise, in case 3 the observer's line of sight vector fully passes through the eclipsed region. In this case, Equation (43) has two valid solutions which correspond the range along the line of sight vector that transitions from sun lit to eclipse and the range that transitions from eclipse to sun lit. Case 4 considers the remaining condition where the line of sight vector transitions from sun lit to eclipse far from the observer. The constraint is shown on the admissible region plot at approximately $\rho = 4$. These test cases prove that the addition of the illumination constraint further reduces the size of the admissible region. The addition of the inclination constraint is shown in Figure . These contour plots represent the different inclinations possible for a given $(\rho, \dot{\rho})$. If the possible inclinations of an object are known, then the inclination constraint significantly reduces the admissible region for the target object.

CONCLUSIONS

This paper has presented a tool capable of simulating the Earth orbit environment based on measurements of known and tracked objects. In order to aid in the mission design process for space surveillance missions such as the RECONSO mission or the Georgia Tech Raven-class telescope,

Table 1. Case Descriptions for Admissible Regions

Case	r_x	r_y	r_z	$\dot{r}_x$	$\dot{r}_y$	$\dot{r}_z$	$r_{o,x}$	$r_{o,y}$	$r_{o,z}$	$\dot{r}_{o,x}$	$\dot{r}_{o,y}$	$\dot{r}_{o,z}$
1	2	-1	-0.750	0.460	-0.460	0	1	-1	-1	0.537	-0.537	0
2	2	2	2	-0.380	0.380	0	1	0	0	0	0	0
3	2	2	2	-0.380	0.380	0	1	-1	-1	0.537	-0.537	0
4	2	-0.778	-0.778	0.468	0.468	0	-1	-1	-1	0.537	-0.537	0

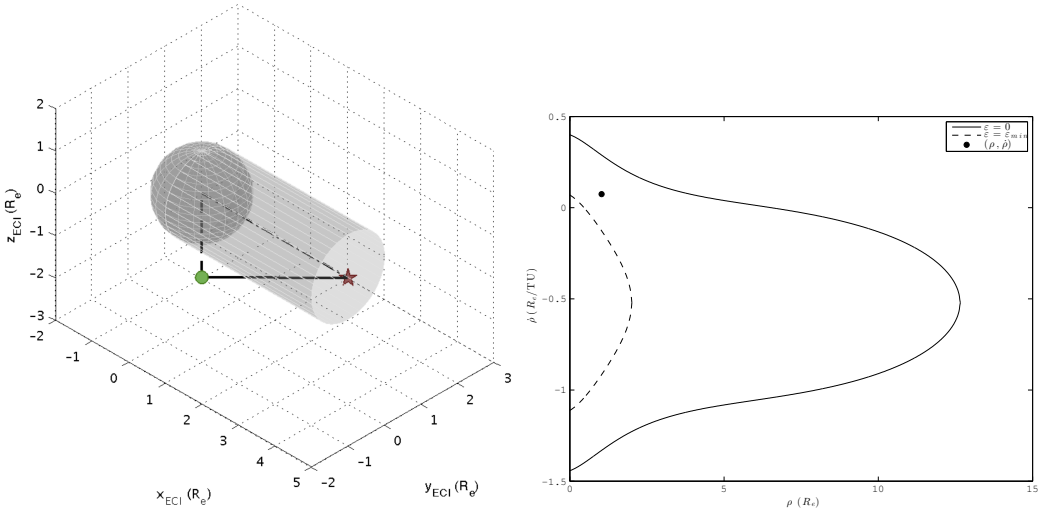

(a) Visualization (b) Admissible Region

Figure 11. Case 1: No Eclipse. The green sphere is the observer and the red star is the target space object.

these objects were analyzed for detectability based on LOS, illumination, and visual magnitude. Analysis of the detectability revealed a dependence on range which is used to impose further constraints on the admissible region. As future work, the simulation can be expanded using models of the unknown debris population in order to determine optimum pointing for high regions of detection and observation of new, untracked objects. The state estimation of the new objects can then be assisted by imposing these new constraints on the admissible region providing better initial estimates of the object's orbit and trajectory.

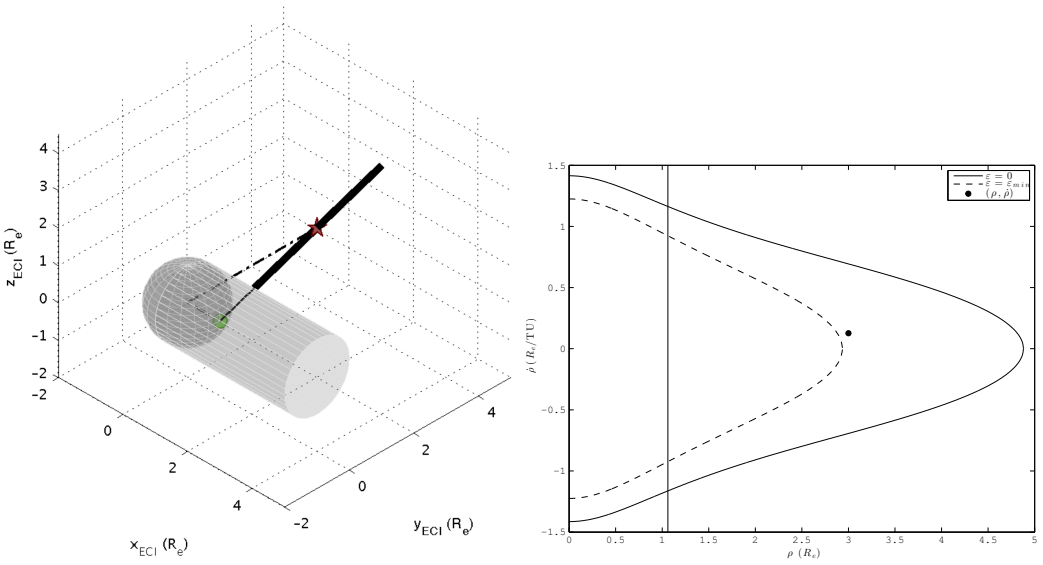

(a) Visualization (b) Admissible Region

Figure 12. Case 2: Near-field Eclipse

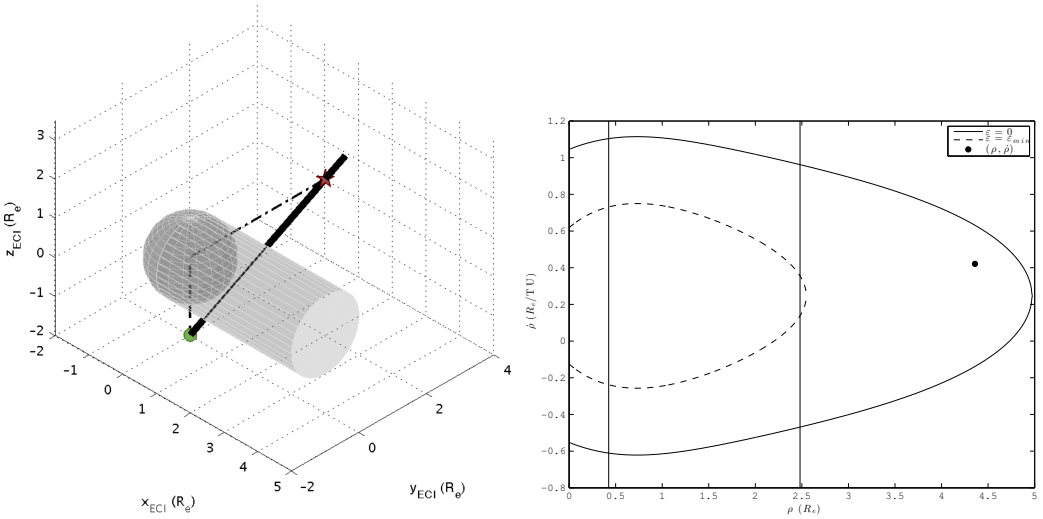

(a) Visualization (b) Admissible Region

Figure 13. Case 3: Intermediate Eclipse

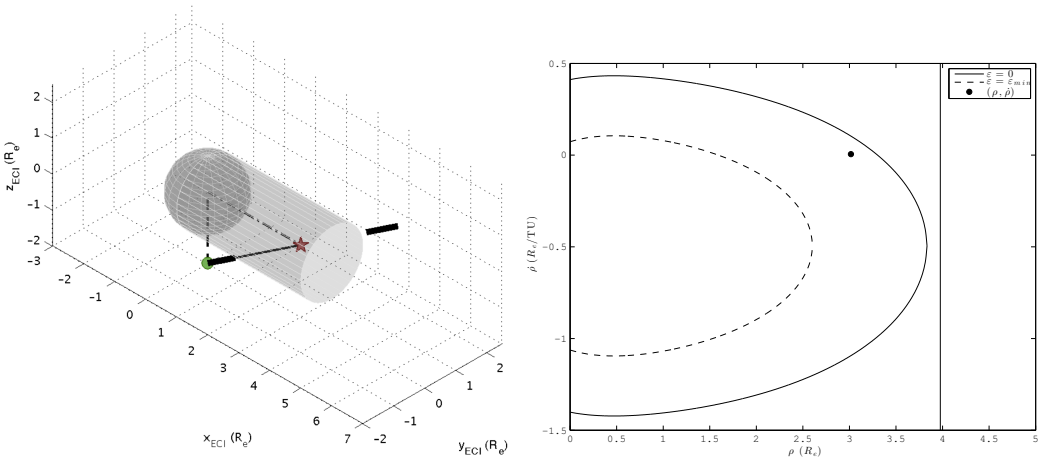

(a) Visualization (b) Admissible Region

Figure 14. Case 4: Far-field Eclipse

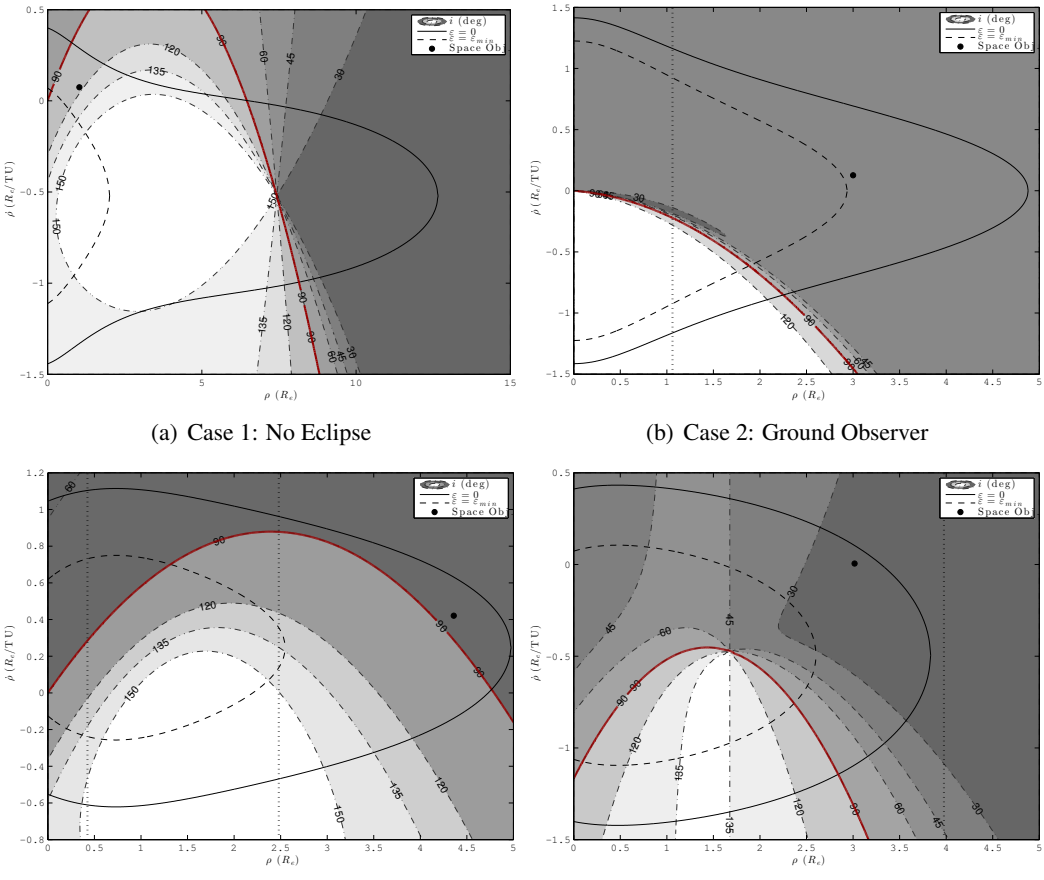

(a) Case 1: No Eclipse (b) Case 2: Ground Observer

(c) Case 3: Intermediate Eclipse (d) Case 4: Far-field Eclipse

Figure 15. Admissible Regions with Eclipse Illumination and Inclination Constraints.

REFERENCES

[1] NASA, "Handbook for Limiting Orbital Debris," 2008.

[2] T. Schildknecht, M. Ploner, and U. Hugentobler, "The search for debris in GEO," *Advances in Space Research*, Vol. 28, No. 9, 2001, pp. 1291 – 1299, http://dx.doi.org/10.1016/S0273-1177(01)00399-4.

[3] Committee on Space Debris, "Orbital Debris: A Technical Assessment," 1995.

[4] "The Threat of Orbital Debris and Protecting NASA Space Assets from Satellite Collisions," 2009.

[5] D. S. McKnight and F. R. D. Pentino, "New insights on the orbital debris collision hazard at GEO," *Acta Astronautica*, Vol. 85, No. 0, 2013, pp. 73 – 82, http://dx.doi.org/10.1016/j.actaastro.2012.12.006.

[6] M. Matney, "Small Debris Observations from the Iridium 33/Cosmos-2251 Collision," *Orbital Debris Quarterly News*, Vol. 14, No. 2, 2010, pp. 6–8.

[7] E. M. Gaposchkin, C. v. Braun, and J. Sharma, "Space-based space surveillance with the space-based visible," *Journal of Guidance, Control, and Dynamics*, Vol. 23, No. 1, 2000, pp. 148–152.

[8] R. D. Coder and M. J. Holzinger, "Autonomy Architecture for a Raven-Class Telescope with Space Situational Awareness Applications," *2013 AAS/AIAA SFM Conference*, 2013.

[9] K. Fujimoto and D. J. Scheeres, "Applications of the Admissible Region to Space-Based Observations," *Advances in Space Research*, 2013.

[10] J. M. Maruskin, D. J. Scheeres, and K. T. Alfriend, "Correlation of optical observations of objects in earth orbit," *Journal of Guidance, Control, and Dynamics*, Vol. 32, No. 1, 2009, pp. 194–209.

[11] J. Shell, "Optimizing orbital debris monitoring with optical telescopes," *Advanced Maui Optical and Space Surveillance Technologies Conference*, Sept. 2010.

[12] W. E. Krag, "Visible magnitude of typical satellites in synchronous orbits," *NASA STI/Recon Technical Report N*, Vol. 75, Sept. 1974, p. 12024.

[13] M. Mulrooney, M. J. Matney, M. D. Hejduk, and E. S. Barker, "An Investigation of Global Albedo Values," *Proceedings of the Advanced Maui Optical and Space Surveillance Technologies Conference*, 2008.

[14] A. Milani, G. F. Gronchi, M. d. Vitturi, and Z. Knežević, "Orbit determination with very short arcs. I admissible regions," *Celestial Mechanics and Dynamical Astronomy*, Vol. 90, No. 1-2, 2004, pp. 57–85.

[15] G. Tommei, A. Milani, and A. Rossi, "Orbit determination of space debris: admissible regions," *Celestial Mechanics and Dynamical Astronomy*, Vol. 97, No. 4, 2007, pp. 289–304.

[16] K. J. DeMars and J. K. Moriba, "Initial orbit determination via gaussian mixture approximation of the admissible region," *2012 AAS/AIAA SFM Meeting*, 2012.

[17] D. A. Vallado and P. Crawford, "SGP4 orbit determination," *Proceedings of AIAA/AAS Astrodynamics Specialist Conference and Exhibit*, 2008, pp. 18–21.

[18] R. L. R. Felix R. Hoots, "Models for Propagation of NORAD Element Sets," tech. rep., 1980.

[19] JPL , "JPL's HORIZONS System," Webpage, Nov. 2005.

[20] A. Pcsi, "An Oblique Hammer Projection," *The Professional Geographer*, Vol. 18, No. 4, 1966, pp. 235–235, 10.1111/j.0033-0124.1966.00235.x.